Wildfires heat the middle troposphere over the Himalayas and Tibetan Plateau during the peak of fire season

Qiaomin Pei [1], Chuanfeng Zhao [1,2] *, Yikun Yang [1], Annan Chen [1], Zhiyuan Cong [3], Xin Wan [4], Haotian Zhang [1], Guangming Wu [5]

1 Department of Atmospheric and Oceanic Sciences, School of Physics, Peking University, Beijing 100871, China.

2 Institute of Carbon Neutrality, Peking University, Beijing 100871, China.

3 School of ecology and environment, Tibet University, Lhasa 850000, China

4 State Key Laboratory of Tibetan Plateau Earth System, Resources and Environment (TPESRE), Institute of Tibetan Plateau Research, Chinese Academy of Sciences, Beijing 100101, China

5 National Institute of Natural Hazards, Ministry of Emergency Management of China, Beijing 100085, China

* Correspondence to: Chuanfeng Zhao (cfzhao@pku.edu.cn)

Abstract

Atmospheric pollution from biomass burning contributes to climatic and cryospheric changes by influencing solar radiation and the albedos of snow and ice surfaces over the Himalayas and Tibetan Plateau (HTP). We utilize long-term MODIS fire products together with ground-based and satellite-derived aerosol datasets to assess the primary effect of wildfires originating from the southern slopes of Himalayas on aerosol loading in the HTP. Results reveal consistent interannual and seasonal variation patterns, accompanied by statistically significant correlations between AOD at 500 nm from AERONET stations (Pokhara, QOMS, Nam Co) and Himalayan fires. CALIPSO data further indicate elevated smoke aerosol extinction coefficients at altitudes of 6 to 8 km (middle troposphere) in the southern HTP during the peak fire season (March–April) in 2021. The intense wildfire activity in 2021 likely induced mid-tropospheric warming and alterations in the vertical temperature structure, evidenced by a pronounced reduction in the absolute lapse rate, representing the rate of temperature decrease with altitude. This reduction was observed at QOMS, SETS, and Naqu stations compared to 2022. SBDART simulations estimated increased heating rates (0.38–1.32 K day^{-1}) and atmospheric warming (15.03–22.43 W m^{-2}) in the mid-troposphere due to smoke aerosols. Such warming affects regional atmospheric stability and modulates surface temperatures (~0.04 K). It is crucial to conduct further research into the heating/cooling processes induced by aerosols and their influence on the vertical temperature structure to comprehensively understand the impacts of aerosols on regional climate and the hydrological cycle.

1   Introduction

Continued global warming is driving widespread and rapid changes in the atmosphere, oceans, cryosphere, and biosphere (IPCC, 2023a). Aerosols in the atmosphere act as one of the main roles in global climate change. Aerosols can impact the Earth's radiative energy budget by altering the scattering and absorption of incoming solar radiation, as well as by affecting cloud properties, including both cloud micro- and macro-physics (IPCC, 2023b). Specifically, these aerosol effects can lead to large reductions in the amount of solar irradiance reaching Earth's surface, a corresponding increase in solar heating of the atmosphere, and changes in the atmospheric temperature structure (Ramanathan et al., 2001a; Koren et al., 2004). The annual mean aerosol-induced atmospheric heating was observed to be considerable, exceeding 0.5 K day^{-1} over Asia (Ramachandran et al., 2020), with values ranging from 0.5 to 0.8 K day^{-1} over the Hindu Kush-Himalaya-Tibetan Plateau region (Ramachandran et al., 2023). This significant aerosol-induced warming has profound implications for both the climate system and the hydrological cycle (Ramachandran et al., 2020).

The Tibetan Plateau and adjacent mountain ranges (including Himalayan, Hindu Kush and Karakoram) are named the Third Pole because they comprise the largest global store of frozen water outside the polar regions (Yao et al., 2022). It functions as a water distribution system termed the Asian Water Tower (AWT), providing a reliable water supply to almost 2 billion people (Yao et al., 2022; Immerzeel et al., 2010). Snow and glacier melting are crucial hydrologic processes and primary sources of headwater in these areas, which are highly affected by temperature and precipitation changes linked to climate change (Immerzeel et al., 2010). However, the Himalayas and Tibetan Plateau region (HTP) is sensitive and prone to climate change, experiencing amplified warming at twice the rate of the global average (Krishnan et al., 2019; Chen, 2015). Marked atmospheric warming is leading to strong cryosphere melt and intensification of the water cycle, which is accompanied with a changing environment and ecosystem (Yao et al., 2019). Meanwhile, black carbon (BC) dominates the aerosol absorption over this region (Ramachandran et al., 2020), along with the dust aerosols (Zhao et al., 2020), and its records show a continuous increase since the 1850s in the Tibetan Plateau (Kang et al., 2020). The elevated levels of BC can further enhance regional warming and contribute to an increase in snowmelt and ice discharge (Kang et al., 2020;

65   Ramachandran et al., 2020).

66   The high BC concentrations over the HTP region were attributed to air pollution transported

67   from South Asia in the previous studies (Li et al., 2016; Lüthi et al., 2015). The northern part of

68   South Asia is known to be the regional hotspot of atmospheric brown clouds (ABCs) (Ramanathan

69   et al., 2007), characterized by high aerosol optical depth (AOD) (Figure S1), which are mostly the

70   result of biomass burning and fossil fuel combustion (Ramanathan et al., 2001b). These polluted air

71   masses on the southern side of the Himalayas can be cross-border transported to the Tibetan Plateau

72   via the combination of the westerlies and Indian monsoon (Lüthi et al., 2015; Kang et al., 2019).

73   This phenomenon is substantiated by the presence of elevated concentrations of nitrogenous

74   aerosols (Bhattarai et al., 2023) and carbonaceous aerosols (Cong et al., 2015) on the southern edge

75   of the Tibetan Plateau in the pre-monsoon period (March−May). In particular, biomass burning

76   emissions from South Asia contributed up to 90% of BC mass over the Tibetan Plateau during the

77   pre-monsoon season (Yang et al., 2021a). The biomass burning mainly includes the forest fires on

78   southern slope of the Himalayas (along the Himalayas in India and Nepal) and agricultural residue

79   burning in the Indo-Gangetic Plain (Figure 1), both of which are generally pronounced in April

80   every year (Vadrevu et al., 2012; Venkataraman et al., 2006). Aerosols emitted from vegetation

81   burning sources are concentrated in the fire season (October/November to May) along the

82   Himalayas in India and Nepal (Vadrevu et al., 2012; Venkataraman et al., 2006), with more than 80%

83   of the wildfires occurring from March to May (Bhardwaj et al., 2016; You et al., 2018).

84   More frequent wildland fires over the India and Nepal Himalayas were observed in recent years

85   as a result of climate and land use changes (You and Xu, 2022; Vadrevu et al., 2012; You et al.,

86   2018). The enhanced BC concentrations from more frequent wildfires in the region may further

87   affect meteorological elements (Yang et al., 2021a) and destabilize the atmosphere over the

88   Himalayas (You and Xu, 2022). The reduction in net radiation at the near-surface layer caused by

89   BC was reported to range from 8 to 16 W m^{-2} over the Tibetan Plateau (Yang et al., 2021a). Aerosols

90   originating from South Asian biomass burning were estimated using WRF-Chem (Weather Research

91   and Forecasting model coupled with Chemistry), resulting in a surface temperature decrease of 0.06°C

92   over the Tibetan Plateau during the pre-monsoon season (Yang et al., 2023). Aerosol effects

93   characterized by high aerosol radiative forcing efficiency and high atmospheric heating rates have

also been observed, accounting for >50% of total warming (aerosols + greenhouse gases) of the lower atmosphere and surface over the HTP region (Ramachandran et al., 2023). Aerosol-induced atmospheric warming can modify regional atmospheric stability and vertical motions, influence large-scale circulation patterns, and disrupt the hydrological cycle, leading to substantial regional climate effects and subsequent impacts (Menon et al., 2002). The 'heat-pump' effect of the Tibetan Plateau (Wu et al., 2007) could be enhanced by this warming, potentially intensifying convection and precipitation in the Tibetan Plateau and downstream regions (Lau and Kim, 2018; Zhao et al., 2020). Therefore, it is essential to further evaluate the implications of vertical temperature profiles induced by biomass burning aerosols from South Asia. This is a key factor driving climate change and shaping the hydrological cycle and precipitation patterns over the HTP region (Ramachandran et al., 2023).
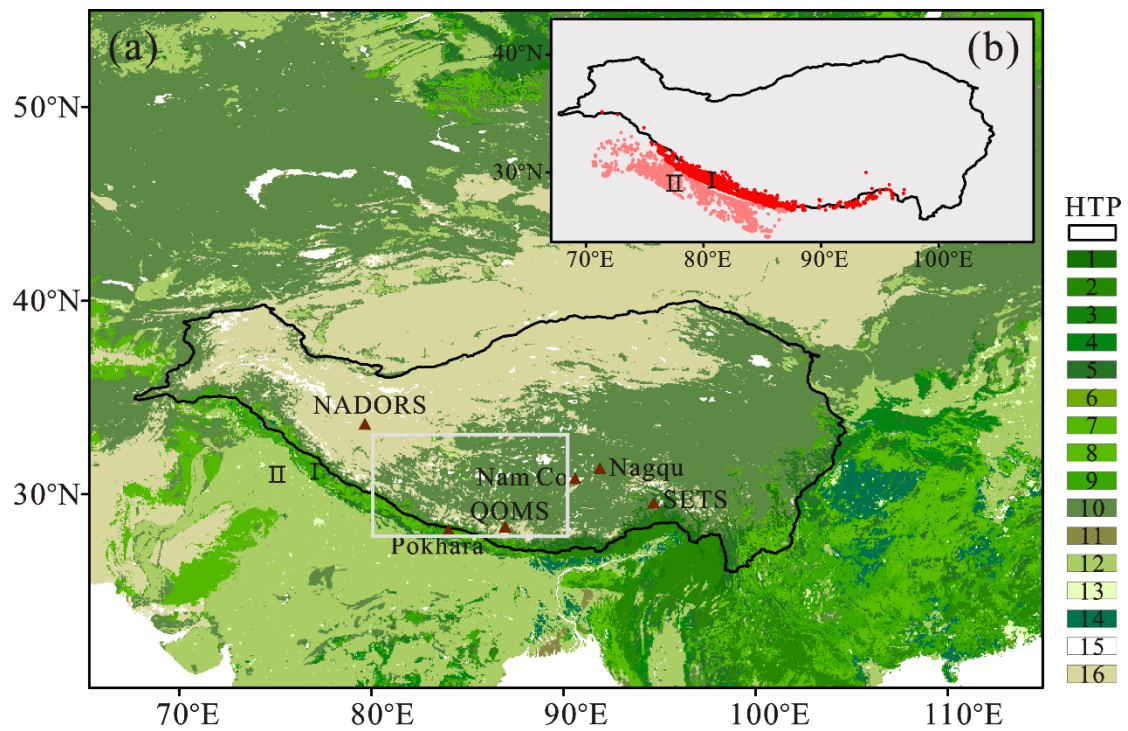
Figure 1. Locations of AERONET and MWR stations (Table S1) overlaid with vegetation distribution (a) and fire pixel counts on April 16, 2021, in the two primary biomass burning regions: forest fires in the Himalayas (Region I) and agricultural residue burning in the Indo-Gangetic Plain (Region II) (b). Vegetation categories: 1–5, Forest; 6–7, Shrublands; 8–9, Savannas; 10, Grasslands; 11, Permanent Wetlands; 12, Croplands; 13, Urban and Built-up Lands; 14, Cropland/Natural Vegetation; 15, Permanent Snow and Ice; 16, Barren.

Most studies have focused on observing the influence of biomass burning from South Asia on the HTP in the last decade. However, there have been limited detailed investigations into

distinguishing between the different biomass burning sources, such as agricultural residue burning and wild forest fires, as well as their potential impacts on atmospheric heating over the HTP. This study utilizes multi-year aerosol products from ground-based observations (AErosol RObotic NETwork, AERONET), fire point information from satellite data (Moderate Resolution Imaging Spectroradiometer, MODIS), and the HYSPLIT (HYbrid Single-Particle Lagrangian Integrated Trajectory) model to investigate the primary biomass burning sources influencing the HTP. In addition, this paper provides observational evidence for biomass burning aerosol-induced atmospheric warming in the middle troposphere during fire events over the HTP, using a combination of ground-based measurements (microwave radiometer instrument), satellite-based data (e.g., Cloud-Aerosol Lidar and Infrared Pathfinder Satellite Observation, CALIPSO; Clouds and the Earth's Radiant Energy System, CERES) and modeling tool (Santa Barbara DISORT Atmospheric Radiative Transfer, SBDART). This study presents a pioneering, state-of-the-art analysis of the vertical profile of atmospheric warming associated with the transport of biomass burning aerosols, a crucial aspect for understanding aerosol-atmosphere interactions and aerosol-climate implications over the HTP region.

2 Data and Methods

2.1 Measurement stations

The Nam Co Station for Multisphere Observation and Research, Chinese Academy of Sciences (Nam Co) is located on the southeastern banks of the Nam Co Lake and in the central part of Tibetan Plateau. The geographic characteristics of Nam Co region include mountains, glaciers, lakes, rivers, and grassland, and thus can be considered representative of the diversity of Tibetan Plateau (Wu et al., 2018). The Qomolangma (Mt. Everest) Station for Atmospheric and Environmental Observation and Research, Chinese Academy of Sciences (QOMS) is located at the southern edge of the Tibetan Plateau and at the foot of Mount Everest. Glaciers and high mountain peaks are close to this region (Li et al., 2020). The Pokhara Valley (Pokhara) in the central Himalayas is one of the major metropolitan regions at the foothills of the Hindu Kush Himalaya mountains in Nepal (Ramachandran et al., 2023). QOMS and Pokhara can be taken as representative sites for the Himalayas. Additionally, stations with microwave radiometer (MWR) installed include Ngari

142   Desert Observation and Research Station, Chinese Academy of Sciences (NADOR), QOMS, the

143   Naqu Station of Plateau Climate and Environment, Chinese Academy of Sciences (Naqu), and the

144   South-East Tibetan plateau Station for integrated observation and research of alpine environment,

145   Chinese Academy of Sciences (SETS). These stations are distributed across various regions of

146   Tibetan Plateau, primarily covering the southern and central areas (Figure 1 and Table S1).

147   **2.2 Ground-based data**

148   The level 2.0 quality-controlled and cloud-screened data of the aerosol spectral deconvolution

149   algorithm (SDA) AOD, particle volume size distribution (dV(r)/dlnr), single-scattering albedo

150   (SSA), and aerosol radiative forcing (ARF) from AERONET version 3 are used in this study. The

151   NASA AERONET is a worldwide ground-based observation network providing long-term and high-

152   quality datasets of aerosol optical, microphysical, and radiative properties. An automatic sun/sky

153   scanning radiometer (CIMEL) measured the solar radiation with a 1.2° full field of view every 15

154   min at 340, 380, 440, 500, 675, 870, and 1,020 nm channels plus a 940 nm water vapor band (Holben

155   et al., 1998). The AERONET retrieved aerosol properties have the highest accuracy for observations

156   when the solar zenith angle is between 50° and 80° (Dubovik et al., 2000), and only the data points

157   in a day that are within this solar zenith angle range are chosen for analyses in the study. The

158   uncertainty of AERONET direct measurement AOD is less than ±0.01 for wavelengths > 0.44 μm

159   and is less than ±0.02 for shorter wavelengths (Holben et al., 2001). The error in single-scattering

160   albedo (SSA) is ±0.03 when the AOD at 0.44 μm is >0.2, and errors in the estimates of particle

161   volume size distribution (dV(r)/dlnr) are less than one tenth of the maximum dV(r)/dlnr values

162   (Dubovik et al., 2000). AERONET ARF values derived for the broadband solar spectrum (0.2–4 μm)

163   are quality controlled, cloud screened, calibrated, and retrieved for clear-sky atmosphere, and for

164   aerosols present in the column (Ramachandran et al., 2023). To ensure that the effect of surface

165   albedo on ARF can be neglected, the spectral average of the surface albedo in the wavelength range

166   of 0.44–1.02 μm is selected to be less than 0.3 for all the sites in the study. Data from all available

167   AERONET sites in the study area (Figure 1 and Supplementary Table 1) are used for validation.

168   These datasets are available for free from the AERONET website. Level 1.5 data are used for the

169   period from June 2022 to June 2024 at Pokhara and from September 2017 to May 2024 at Nam Co,

170   respectively, due to the unavailability of Level 2.0 data.

The temperature profiles at QOMS, SETS, Naqu and NADORS in 2021 and 2022 were measured by MWR operating in the K- and V-bands (20–60 GHz) (Ma Yaoming, 2024), which are sensitive to the low part of the atmosphere. The microwave radiometers instrument was an MWP967KV temperature, humidity, and liquid profiler, which operates with eight K-band (22.235, 22.50, 23.035, 23.835, 25.00, 26.235, 28.0, and 30.0 GHz) and fourteen V-band (51.25, 51.760, 52.28, 52.8, 53.34, 53.85, 54.4, 54.94, 55.50, 56.02, 56.66, 57.29, 57.96, and 58.80 GHz) microwave channels. It measures the radiation intensity of the sky in 22 different frequency channels. Only the zenith scan data are used to retrieve the thermodynamic profiles of the troposphere up to 10 km, which are normally available every 2 minutes. And the details of data information and quality can be found in Chen et al. (2024).

2.3 Satellite data

The MODIS active fire products are determined using thermal anomalies at 1 km pixels that are burning at the time of overpass under relatively cloud-free conditions using a contextual algorithm. The fire pixel counts and fire radiative power (FRP) covering the Himalayas and Indo-Gangetic Plain regions from NASA, with a confidence level greater than 50% from January 2011 to June 2024, are used to explore their relationship with AOD.

The Cloud-Aerosol Lidar and Infrared Pathfinder Satellite Observation (CALIPSO) was launched in April 2006 equipped with Cloud-Aerosol Lidar with Orthogonal Polarization (CALIOP) and observes global aerosol and cloud vertical distributions at 532 and 1064 nm during both day and night (Winker et al., 2010), which provides the aerosol classification from backscatter and depolarization measurements plus some geographical constraints (Omar et al., 2009). The CALIOP level 2 aerosol classification and lidar ratio selection algorithm define six aerosol types: clean marine, dust, polluted continental, clean continental, polluted dust, and smoke (Omar et al., 2009). In this study, the vertical feature mask (VFM) data and Aerosol Profile data from Level 2 profile product Version 4 are used to obtain information about the aerosol/cloud features and aerosol types over the HTP region. Owing to the availability of CALIPSO data through June 2023, our analysis covers the period from 2011 to 2023.

The Clouds and the Earth's Radiant Energy System (CERES) Synoptic Radiative Fluxes product (SYN1deg, edition 4.1) is used to derive the change in the aerosol radiative effect. In the

CERES SYN product, radiative transfer calculations are performed using aerosol properties from the Model for Atmospheric Transport and CHemistry (MATCH), which are constrained by observations from MODIS and CERES. Two flux modes are employed: pristine (clear, no aerosols) and clear sky (clear, with aerosols and cloud-free skies) conditions, both at the surface (SFC) and top of atmosphere (TOA) (Ramachandran et al., 2023). ARF is defined as the perturbation of the radiative flux caused by atmospheric aerosols (Dumka et al., 2016). The ARF_{toa} is estimated by calculating the difference between the net clear-sky and net pristine-sky fluxes at the top of atmosphere, and the ARF_{atm} (atmospheric forcing) is determined as the difference between ARF_{toa} and ARF_{sfc} (Ramachandran et al., 2023).

2.4 SBDART model and HYSPLIT

SBDART is based on the discrete ordinate approach developed by the University of California, Santa Barbara (Ricchiazzi et al., 1998). The discrete ordinate method is employed to solve the radiative transfer equation for monochromatic, unpolarized radiation within a plane-parallel medium that exhibits scattering, absorption, and emission properties, with a defined bidirectional reflectance at the lower boundary (Stamnes et al., 2000). The SBDART model enables the simulation of plane-parallel radiative transfer for both clear and cloudy atmospheric conditions, spanning the region between the Earth's surface and the top of the atmosphere, including the vertical distribution of aerosols and the heating rates (Rai et al., 2019; Kedia et al., 2010; Dumka et al., 2016; Moorthy et al., 2009). In the present case, the model is run for clear-sky conditions determined in the wavelength range of 0.25–4.0 µm. The mid-latitude winter atmospheric standard profile is selected with input parameters including solar zenith angle, surface temperature and surface albedo. The average values of SSA, asymmetry parameter, extinction and AOD at QOMS in April 2021 (Table S2), derived from AERONET, are utilized as inputs for the SBDART model. Building on the methodology of Moorthy et al. (2009) to estimate the uncertainty in ARF and heating rate, we quantified the uncertainties associated with AOD, SSA and asymmetry parameters. The uncertainties in AOD values, SSA, and asymmetry factor were determined to be ±0.02, ±0.01, and ±0.01, based on empirical data and error analysis. The overall uncertainties in ARF and heating rate calculations using SBDART were approximately 15% and varied between 5% and 15%, respectively, as reported in previous studies on the Central Himalayas and the urban areas of South Asia (Pant et

al., 2006; Panicker et al., 2010).

To track the transport of biomass burning aerosols emitted from the Himalayas and the IGP, we used the HYSPLIT (Version 5.3.0) model to calculate the forward trajectories of the air masses (Stein et al., 2015). The model is driven by the 1°×1° horizontal resolution meteorological fields from the Global Data Assimilation System operated by NOAA. The 72-hours forward trajectories are generated for each source region during the fire events in April and May 2021, with a time resolution of 1 hour and a starting altitude of 500m above ground level.

2.5 Heating rate

The aerosol-induced atmospheric solar heating rate (K day^{-1}) is derived from the aerosol radiative forcing in the atmosphere (ARF$_{atm}$) (Ramachandran et al., 2023), which can be defined as the change between the atmospheric forcing with and without aerosols as:

$$ARF_{toa} = (F_{aerosol}^{toa} - F_{no\ aerosol}^{toa}) \tag{1}$$

$$ARF_{sfc} = \left(F_{aerosol}^{sfc} - F_{no\ aerosol}^{sfc}\right) \tag{2}$$

$$ARF_{atm} = ARF_{toa} - ARF_{sfc} \tag{3}$$

Where ARF$_{toa}$ and ARF$_{sfc}$ are aerosol forcing at the top of atmosphere (TOA) and surface (SFC), F denotes net short-wave radiative flux. Subscript 'aerosol' and 'no aerosol' refer to conditions with and without aerosol. This study also employs clear-sky ARF values retrieved from AERONET measurements at both surface and TOA.

ARF$_{atm}$ in W m^{-2} indicates the amount of radiative flux (energy) due to the presence of aerosols within the atmospheric layers, where positive forcing indicates the warming potential of the atmosphere (Kedia et al., 2010; Rai et al., 2019; Moorthy et al., 2009). The energy which is converted into heat is calculated as heating rate using the following equation:

$$\frac{d_T}{d_t} = \frac{g}{C_p} \times \frac{ARF_{atm}}{\Delta P} \times 24(hr/day) \times 3600(sec/hr) \tag{4}$$

where d$_T$/d$_t$ is the heating rate (K day^{-1}), g is the acceleration due to gravity (9.8 m s^{-2}), C_p is the specific heat capacity of the air (1006 J kg^{-1} K^{-1}), and ΔP is the pressure difference between the elevation of observation site and 10 km above sea level (ASL). This calculation takes into account the mountain peaks in the HTP region, which can reach approximately 9 km ASL (Ramachandran et al., 2023).

3 Results and discussion

3.1 Effect of wildfires on aerosol load over HTP

The AOD represents the vertical integral of aerosol concentration weighted with the effective cross-sectional area of the particles intercepting (by scattering and absorption) the solar radiation at the specific wavelength (Ramanathan et al., 2001a). A long-term record of AOD at 500 nm from AERONET is available for Pokhara (2011−2024), QOMS (2011−2024), and Nam Co (2011−2024), located on the southern slope of the Himalayas, the northern slope of the Himalayas, and within the interior of the Tibetan Plateau, respectively (Figure 1). Despite some missing days and months in the AOD records for certain years, distinct seasonal variations are clearly observed at three sites, with a pronounced annual peak during the period March−May (Figure 2). Meanwhile, a spectral deconvolution algorithm was applied to separate AOD into fine- and coarse-mode AOD (O'neill et al., 2003). Similar annual peaks in fine-mode AOD were observed from March to May; however, no consistent seasonality was found in coarse-mode AOD at any site. Previous studies have demonstrated a similar annual seasonality of total AOD and fine-mode AOD at Nam Co, QOMS and Pokhara (Li et al., 2020; Ramachandran and Rupakheti, 2021), along with background aerosol loading characterized by annually low baseline AOD values of 0.029 at Nam Co and 0.027 at QOMS (Pokharel et al., 2019). Notably, the peaks of AOD and fine-mode AOD vary among the three sites: Nam Co experienced its peak in 2016, QOMS in 2021 and 2024, and Pokhara in 2016 and 2024, with no data available for Pokhara in 2021. During these extreme peaks, the monthly mean AOD increased by 5 to 10 times relative to the baseline values at Nam Co and QOMS, and by up to 50 times at the Pokhara site. This suggests that exogenous aerosols have a more significant influence on the southern slopes of the Himalayas compared to the Tibetan Plateau and the northern slopes of Himalayas.
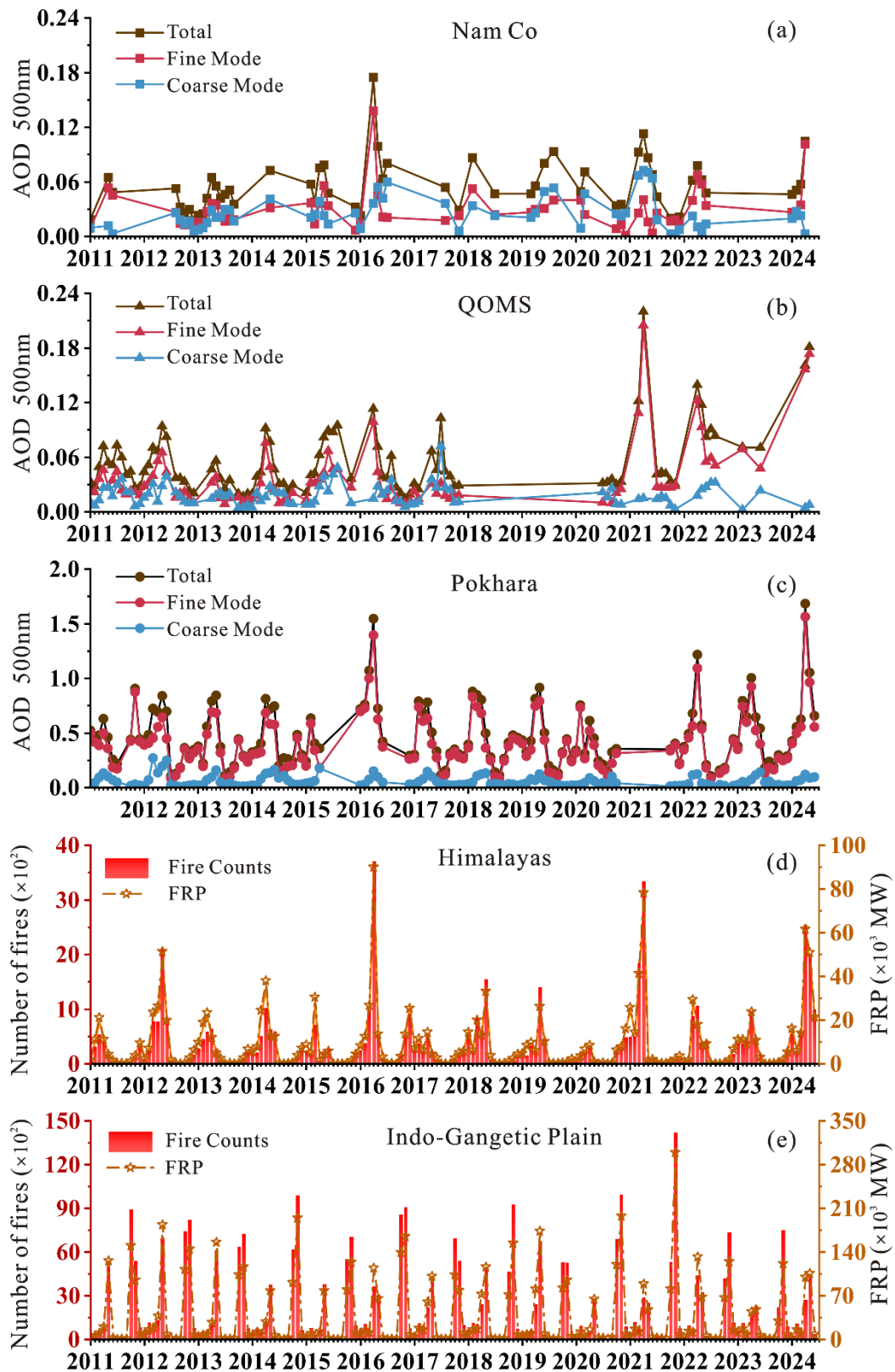
Figure 2. Temporal variations of monthly mean AERONET AOD at 500 nm, fine-mode AOD at 500 nm and coarse-mode at 500 nm at Nam Co (a), QOMS (b), and Pokhara (c); and time series of the monthly average number of fires and FRP from the MODIS Active Fire Product over the Himalayas (d) and Indo-Gangetic Plain (e).

284   The fire pixel counts and FRP values provide information about the fire frequencies and

285   emissions. The monthly total fire pixel counts and FRP from January 2011 to June 2024 over the

286   Himalayas and Indo-Gangetic Plain were detected by MODIS with a confidence level exceeding

287   50%, exhibiting similar interannual and seasonal patterns in both regions (Figure 2). In the

288   Himalayas, fire activity exhibits a single annual peak occurring between March and May, whereas

289   the Indo-Gangetic Plain demonstrates a bimodal pattern with two distinct peaks, one in April/May

290   and the other in October/November, corresponding to the two major harvest seasons (Venkataraman

291   et al., 2006). The fire pixel counts showed notable occurrences during the fire seasons of 2016, 2021,

292   and 2024 in the Himalayas, with total numbers of 5427, 5700 and 5534, respectively. The three

293   peaks in fire pixel counts are consistent with the high concentrations of fine-mode aerosols observed

294   in April at QOMS. In contrast, a relatively high value of fire pixel counts and FRP was observed in

295   November 2021 in the Indo-Gangetic Plain region. The wildfires in the Himalayas exhibit

296   pronounced interannual variability, whereas the interannual fluctuations in the Indo-Gangetic Plain

297   are relatively stable, primarily influenced by anthropogenic agricultural activities (Vadrevu et al.,

298   2012; Kaskaoutis et al., 2014).

299   The long-term temporal variations in the number of active fires and FRP over Himalayas

300   present a distinct consistency with the temporal variations in total AOD and fine-mode AOD, at the

301   Nam Co, QOMS and Pokhara sites (Figure 2). There are significant positive correlations between

302   the fire pixel counts over the Himalayas and AOD at Pokhara ($r = 0.76$, $p < 0.001$), QOMS ($r = 0.71$,

303    $p < 0.001$) and Nam Co ($r = 0.69$, $p < 0.001$) for the whole study period (2011−2024). Additionally,

304   the fine-mode AOD variations at these three sites are also well correlated with fire pixel counts over

305   the Himalayas (Pokhara: $r = 0.73$, $p < 0.001$; QOMS: $r = 0.80$, $p < 0.001$; and Nam Co: $r = 0.68$, p

306   < 0.001; Figure 3). However, a weak relationship exists between the fine-mode AOD at Pokhara

307   and fire pixel counts over the IGP ($r = 0.23$, $p < 0.001$), and no correlation was observed between

308   fire pixel counts over the IGP and fine-mode AOD at both Nam Co and QOMS (Figure 3). Similar

309   influences of forest fires and agricultural residue fires on aerosol properties at Pokhara was

310   investigated by Ramachandran and Rupakheti (2021). In our study, these relationships suggest that

311   the aerosol loading in the HTP region, particularly fine particles, is primarily influenced by wildfires

312   occurring on the southern slopes of the Himalayas. Moreover, the monthly average aerosol volume

size distributions for April from 2011 to 2024 at QOMS are presented in Figure S2. In general, the aerosol particle size distributions show a bimodal lognormal pattern with a radius smaller than 0.6 μm as fine-mode aerosol and with radius larger than 0.6 μm as coarse-mode aerosol (Yang et al., 2021b; Zheng et al., 2017). It is clear that the volume sizes with peak volume concentrations for fine-mode aerosols in April were higher in 2016, 2021, and 2024 than in other years at QOMS (Figure S2). The years characterized by elevated fine-mode aerosol levels correspond to the periods with maximum AOD and fine-mode AOD values discussed in the preceding paragraph. The peak volume concentrations of fine-mode aerosols were the highest in 2021, with values of 0.024 um^3/um^2. The result is consistent with the previous study of biomass burning events at Nam Co and QOMS stations (Pokharel et al., 2019), which supported the prevalence of high fine-mode AOD and fine particles associated with biomass burning during the pre-monsoon. There were also maximum values of fine-mode AOD which were attributed to fine particles generated by biomass burning during extreme fire events in Australia (Yang et al., 2021b). Therefore, this indicates that fine-mode volume concentrations significantly increased during wildfire seasons.

Additionally, 72-hours forward trajectories were obtained via the HYSPLIT model for each of the 30 days in April and May, with starting points at sites located on the southern slopes of the Himalayas and within the IGP region. The results indicate that the Tibetan Plateau predominately receives air masses originating from the southern slopes of the Himalayas in April (accounting for 26 to 28 out of 30 days) and May (approximately 29 out of 30 days), rather than from the IGP region (Figure S3). Additionally, an increase in levoglucosan recorded in the Zangsegangri (ZSGR) ice core from the Tibetan Plateau was also attributed to wildfires, which are associated with the higher FRP levels compared to those from anthropogenic burnings (You et al., 2018). In our study, monthly mean FRP values on the southern slopes of the Himalayas are significantly higher than those from the IGP over the period from 2011 to 2024 (Figure S4). Thus, wildfires occurring on the southern slopes of the Himalayas act as the principal driver of aerosol loading over the HTP region. Various types of biomass sources could exert distinct effects on atmospheric heating over the HTP. We analyze the impacts of wildfires on the HTP during the fire season, whereas the influence of biomass burning from the IGP warrants further detailed investigation in future research.
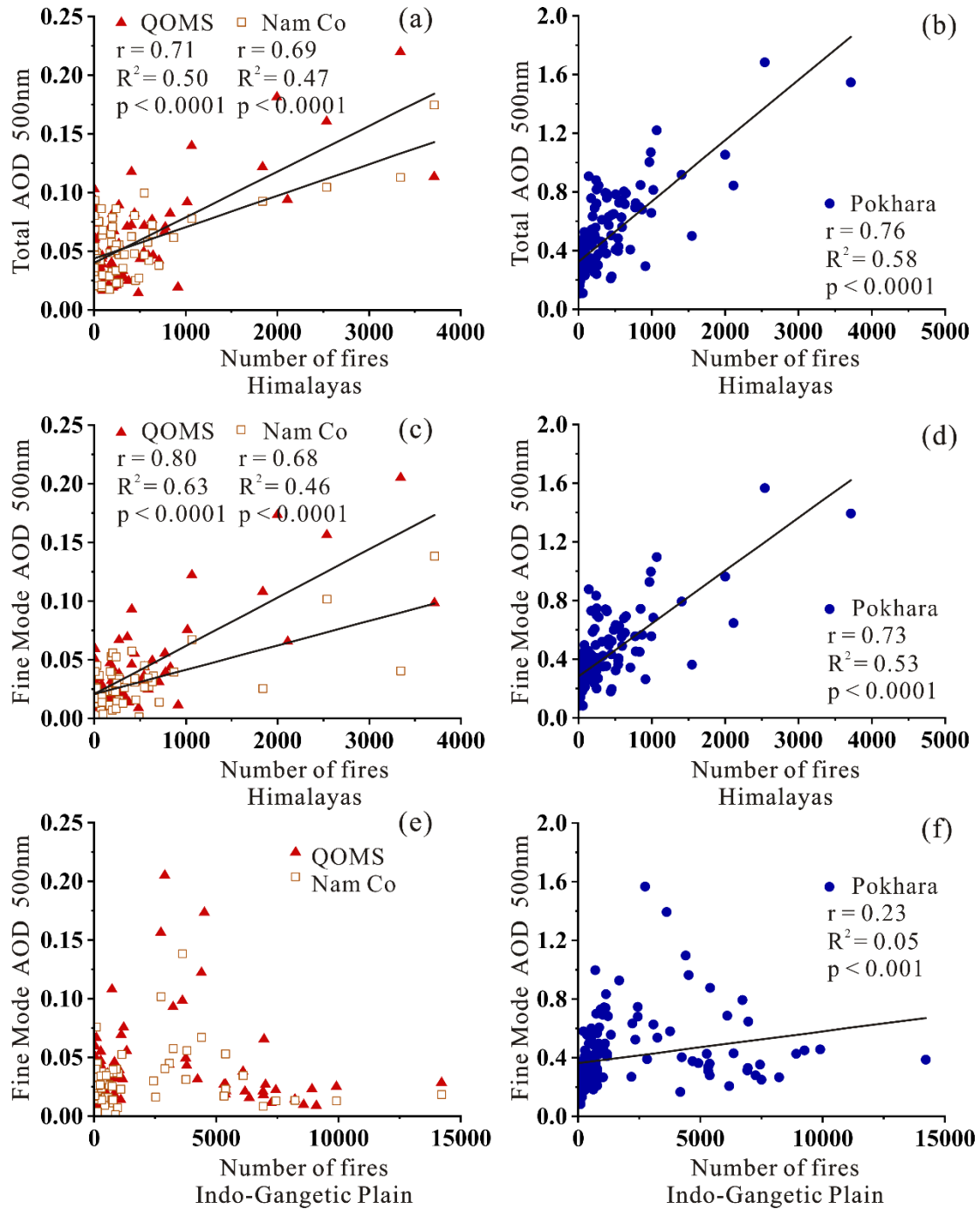
Figure 3. Correlations between monthly AOD at 500 nm at QOMS, Nam Co, and Pokhara and monthly fire pixel counts over the Himalayas (a–d) and the Indo-Gangetic Plain (e–f).

3.2 The increasing temperature in the middle troposphere associated with smoke

The extinction properties of the five aerosol types (dust, smoke, clean continental, polluted dust and polluted continental), along with the annual mean extinction values for all aerosol types from 2011 to 2023 during peak fire season (March and April), were extracted from the CALIPSO L2 aerosol profile product for the selected study domain in the HTP (gray rectangle in Figure 1).

348   The extinction coefficient of smoke aerosols in 2021 was significantly larger than that in other years

349   (Figure 4), which corresponds to the interannual variations in fires across the Himalayas. Figure 5

350   shows the extinction coefficient and occurrence frequency of each aerosol type in March and April

351   from 2021 to 2023 for the same selected region. During the peak of fire season, smoke was abundant

352   at heights from roughly 6 to 8 km and showed a similarly larger extinction coefficient at these

353   heights in 2021 compared to other years. However, the occurrence frequencies of smoke are distinct

354   in different years, which may be correlated with the classes and intensity of wildfires in the

355   Himalayas. Meanwhile, CALIPSO observations taken on 12 April, 15 April, and 28 April 2021 over

356   the HTP region revealed the cloud/aerosol mask and distribution of the aerosol types (Figure 6 and

357   Figure S5). During these observations, smoke was the dominant aerosol type at altitudes between 6

358   and 10 km in the mid-troposphere over the Himalayas and the southern Tibetan Plateau. In specific

359   conditions, mixtures of dust and smoke were frequently classified as polluted dust (Kim et al., 2018;

360   Omar et al., 2009), which verifies the significantly similarity layers between polluted dust and

361   smoke layer on 28 April 2021. The similar vertical distribution of smoke aerosol was also reported,

362   suggesting that wildfire emissions from crown fires in the forest canopy can reach altitudes

363   exceeding 5 km and up to 8–9 km in the mid-troposphere and can sometimes even be uplifted to the

364   free troposphere and lower stratosphere under strong thermal convection in the Himalayas (Vadrevu

365   et al., 2012). Additionally, dust aerosols, as another major aerosol type in the HTP, are identified in

366   Figures 4 and 5. These aerosols are mainly influenced by dust emissions originating from Northwest

367   India and Pakistan, and the plateau itself (Kang et al., 2019; Liu et al., 2008). The temporal variations

368   of dust aerosols are linked to dust events, which are primarily governed by complex factors

369   including surface wind fields, vegetation cover, and the westerly jet (Kang et al., 2016).
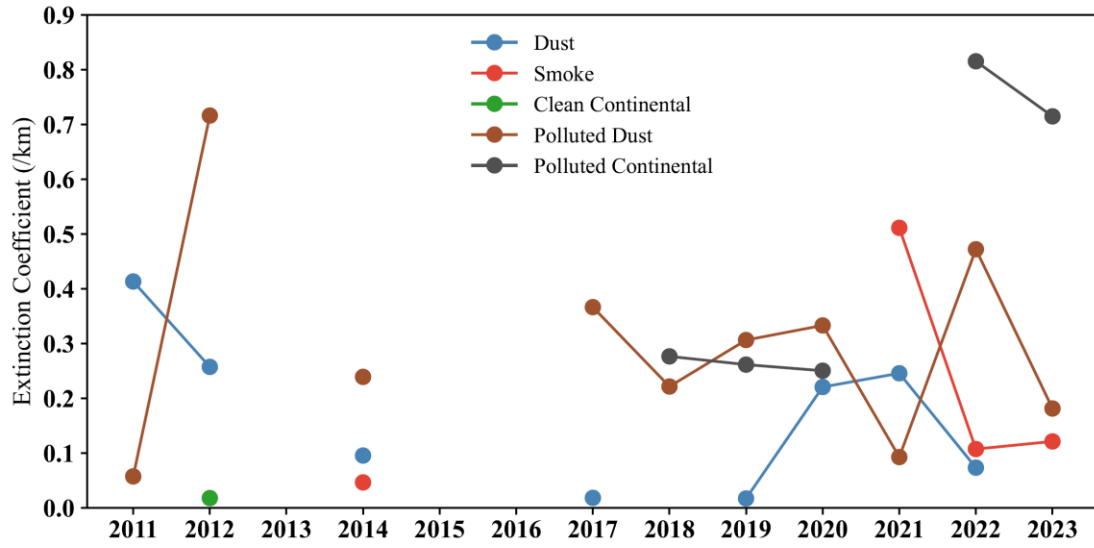
Figure 4. Averaged aerosol extinction coefficient at 532 nm for March and April from 2011 to 2023 over the southern HTP (gray rectangle in Figure 1).
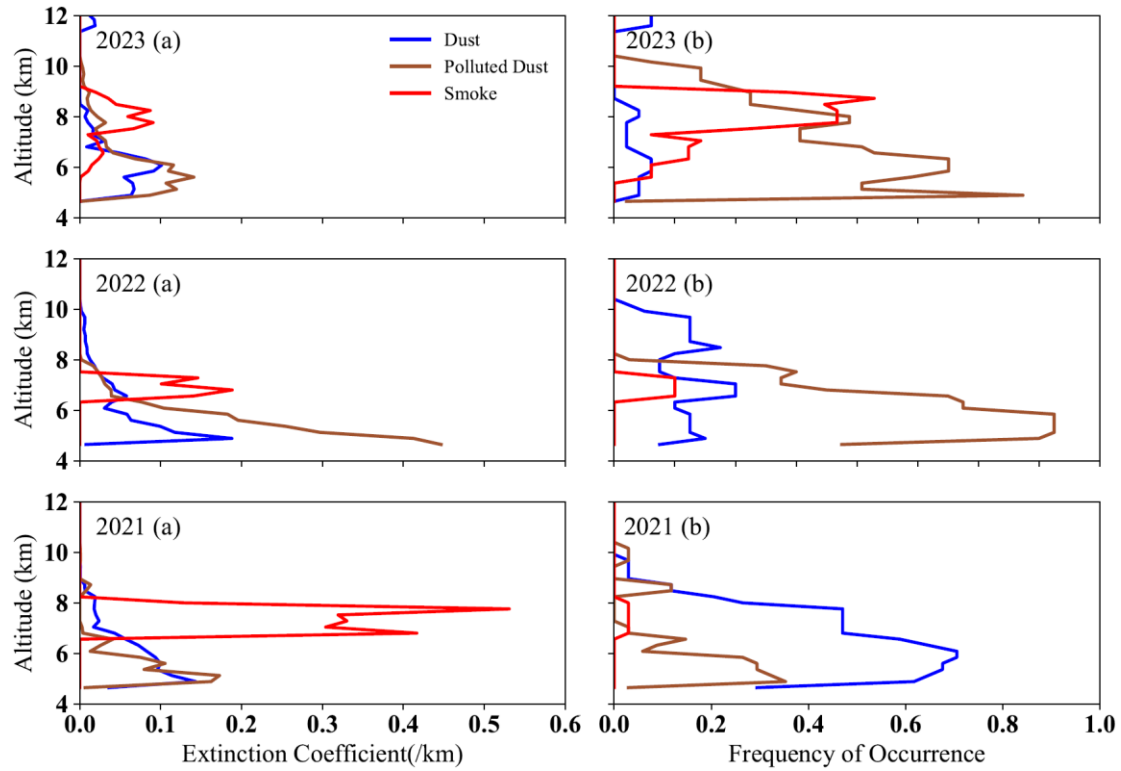
Figure 5. The vertical distribution of averaged aerosol extinction coefficient at 532 nm (a) and occurrence frequency profile of each aerosol type (b) during the peak of the fire season (March and April) from 2021 to 2023 over the southern of HTP (gray rectangle in Figure 1).
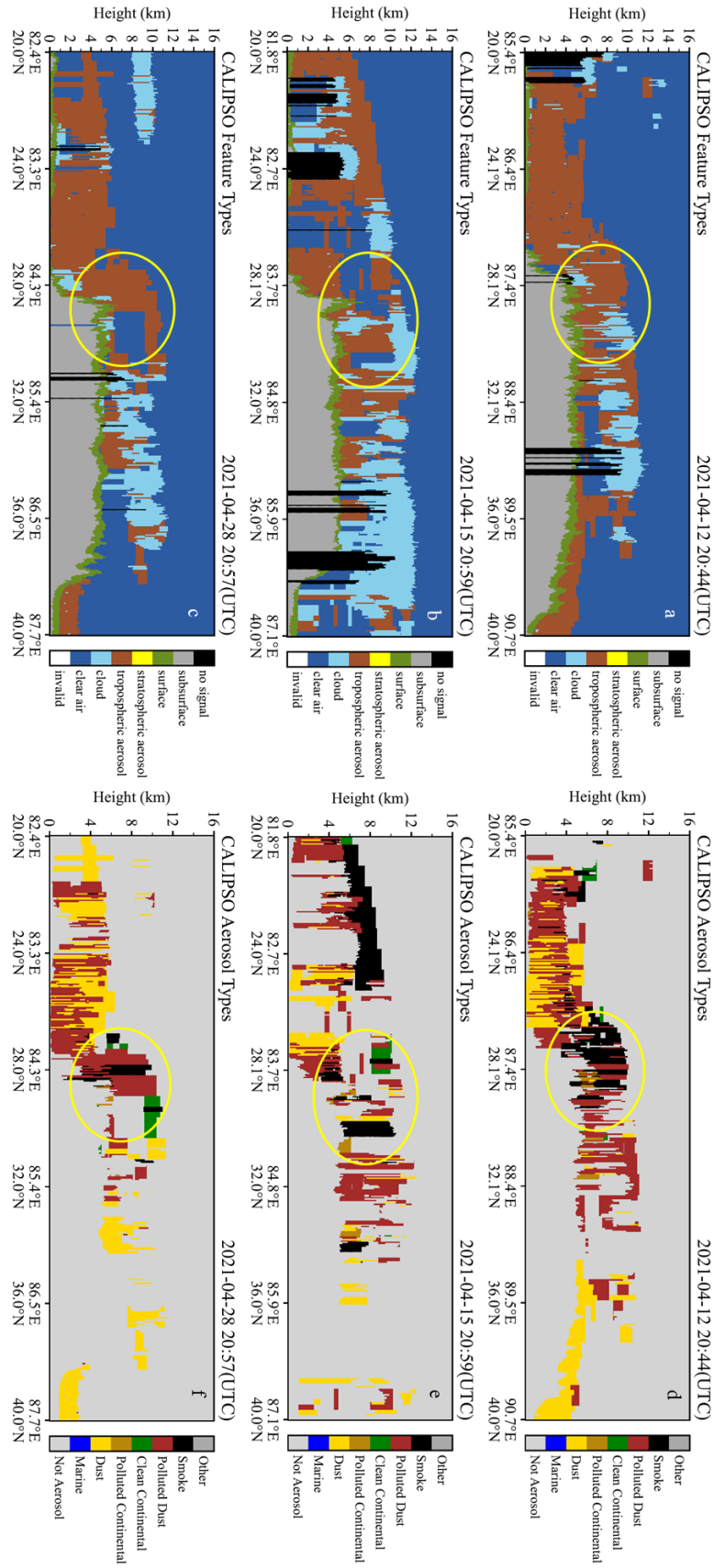
Figure 6. (a–c) Vertical feature mask (VFM) indicating the primary layer type (aerosol or cloud), and (d–f) VFM for aerosol layers, showing aerosol subtypes (CALIPSO observations over the HTP region on April 12, 15, and 28, 2021 in Figure S5).

380   Wildfire smoke particles, mainly consisting of organic carbon (OC) and black carbon (BC)

381   (Andreae, 2019), have the capacity to absorb solar radiation and contribute to stratospheric warming

382   when injected into the stratosphere (Yu et al., 2021; Stocker et al., 2021). Observations and modeling

383   of absorbing aerosols, originating from smoke or urban air pollution, have revealed their ability to

384   warm the atmosphere while reducing the amount of sunlight reaching the Earth's surface (Satheesh

385   and Ramanathan, 2000; Koren et al., 2004). At QOMS, the mean SSA values in April are 0.87, 0.87,

386   0.85, and 0.83 at wavelengths of 0.44μm, 0.675μm, 0.87μm, and 1.02μm (Table S2), respectively.

387   Low SSA values were also detected at Pokhara, with most values around 0.9 (Figure S6), which

388   may be attributed to high BC concentrations (Ramachandran et al., 2020) and indicates a tendency

389   towards a warming effect (Li et al., 2022; Liu, 2005). In addition, the lower SSA values (< 0.8) were

390   measured at observation sites located in the Tibetan Plateau (Wang et al., 2024; Tian et al., 2023),

391   suggesting stronger aerosol absorption and a significant aerosol warming effect. In the study, smoke

392   aerosols were predominantly observed at altitudes between 6 and 8 km in the middle troposphere

393   over the southern HTP area during the peak fire season. We investigated the vertical temperature

394   structure by assessing the rate of decrease in temperature with increasing altitude during March and

395   April for 2021 (a year marked by intense wildfires) and 2022 (a year with relatively weak wildfires).

396   The temperature profiles at QOMS, SETS, and Naqu stations exhibit smaller absolute values of

397   slope K in 2021 compared to those in 2022, excluding the NADOR data (Figure 7). This suggests

398   that the intense wildfire activity influences the temperature structure, resulting in a reduced vertical

399   temperature lapse rate, likely due to the warming effect of smoke in the middle troposphere. As a

400   result of restricted transport pathways (Figure S3), the impact of smoke on the thermal structure is

401   reduced at the NADOR site, which is situated in the southwest of the HTP (Figure 1).

402   To elucidate the effect of smoke layers on the aerosol radiative forcing, we used the realistic

403   CALIPSO smoke extinction profiles (Figure 4) and calculated the heating rates using the SBDART

404   model in both cases, with and without measured vertical profiles (Rai et al., 2019; Kedia et al., 2010;

405   Dumka et al., 2016; Moorthy et al., 2009). The heating rates obtained by including smoke aerosol

406   vertical profiles exhibit structures consistent with aerosol extinction at different altitudes observed,

407   and present higher values than those in the case without aerosol vertical profiles (Figure 8). In the

408   2021 case, the presence of smoke aerosols results in an enhanced atmospheric absorption, leading

to layer warming, with heating rate reaching up to 1.66 ± 0.09 K day^{-1} at the 6 to 8 km level (in the middle troposphere) (Figure 8a). Especially, these heating rates at the smoke layer with different aerosol extinctions exhibit differences, with increases of 0.61–1.32 K day^{-1} in the 2021 case, 0.38–0.67 K day^{-1} in the 2022 case, and 0.51–0.74 K day^{-1} in the 2023 case in the middle troposphere, compared to the scenario without smoke aerosols. The results demonstrate a substantial absorption of solar short-wave radiation by smoke aerosols, which is consistent with the heating rate values (~ 0.5 to 1.9 K day^{-1}) reported in previous studies (Dumka et al., 2016), where a significant contribution of the BC fraction was identified. This is also comparable to previously reported values ranging from 0.45 to 0.7 K day^{-1} due to BC within the so-called "atmospheric brown clouds" (ABCs) between 500 and 3000 m a.s.l. over the Indian Ocean in March 2006 (Ramanathan et al., 2007). The average heating rate of smoke aerosols, modeled by SBDART, is 0.64 ± 0.25 K day^{-1}, which is slightly higher than the mean value for March and April (0.41 ± 0.49 K day^{-1}) from 2011 to 2023 at QOMS, but lower than the corresponding average for March and April (1.13 ± 0.57 K day^{-1}) at Pokhara (Table S3), both of which were retrieved from AERONET. Indeed, the solar heating rates associated with smoke are elevated over the HTP region, as evidenced by both model simulations and observational measurements.

However, the heating rate near the surface (~1.12 K day^{-1}) is less than that (~1.16 K day^{-1}) in the case without smoke aerosol (Figure 8a), indicating a potential cooling of ~0.04 K near the ground. This may be attributed to the reduction in solar radiation reaching the surface due to solar absorption by the smoke layer (Ramanathan et al., 2001a) in the middle troposphere, which subsequently alters air temperature near the ground (Liu, 2005). Here, the net shortwave radiation flux at the surface is notably reduced with the smoke layer compared to the net radiation flux simulated in the absence of smoke aerosol vertical profiles (Figure 8b). The ARF profiles are influenced by the vertical distribution of aerosols, presenting a markedly different pattern in the 2021 case due to the high AOD of the smoke layer (Figure 8c). The ARF above the smoke layer is approximately -14.05 W m^{-2}, -8.94 W m^{-2}, and -9.52 W m^{-2} in the 2021, 2022, and 2023 cases, respectively. The ARF values below the smoke layer are found to be -36.48 W m^{-2}, -23.97 W m^{-2}, and -24.86 W m^{-2} for the same cases, respectively. The average atmospheric warming of the smoke layer is about 15.03 to 22.43 W m^{-2}, suggesting a reduction in solar flux at the surface caused by the absorption of smoke aerosols.

The observed atmospheric warming and heating rates of the smoke aerosols are consistent with the radiative effects (5.85–21.56 W m^{-2}) and heating rates (0.37–1.71 K day^{-1}) of BC from in situ aircraft observations (Lu et al., 2020).
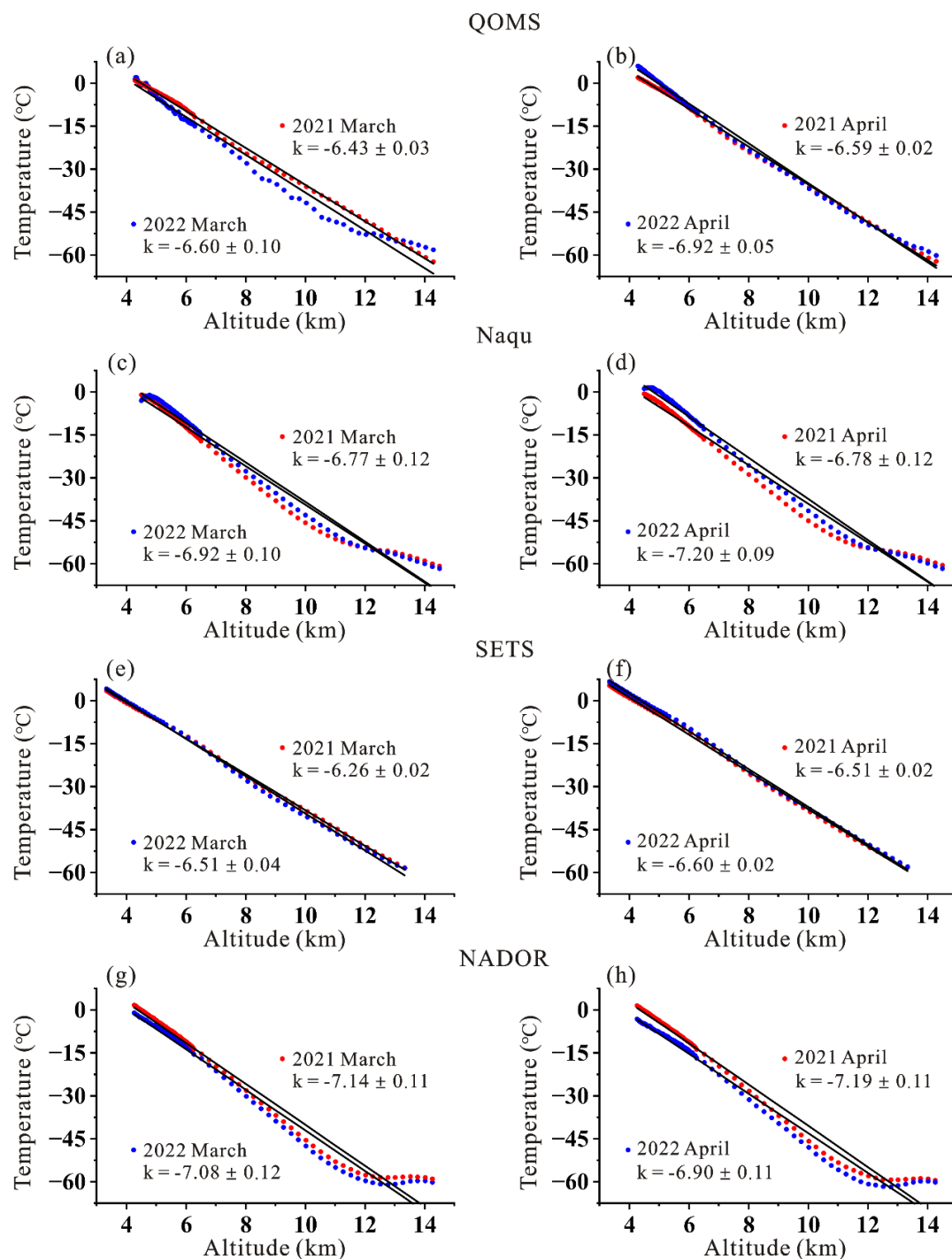
Figure 7. Temperature lapse rates with increasing altitude observed at the QOMS, SETS, Naqu, and NADOR stations during March and April of 2021 and 2022.
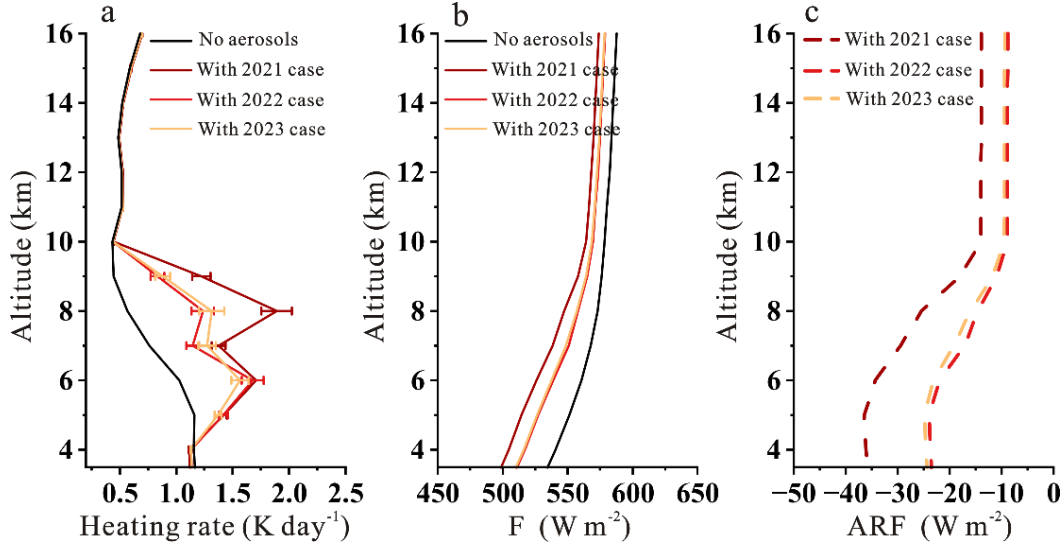
Figure 8. Vertical profiles of heating rate (a), net down radiation flux F (b), and ARF (c) without and with aerosol vertical profiles (2021 case, 2022 case, and 2023 case), simulated with the SBDART model.

Meanwhile, CERES satellite-derived ARF in the atmosphere was studied by Ramachandran et al. (2023), showing positive forcing of atmospheric aerosols over the IGP and Himalayas. In this study, we focus on extreme wildfire events and calculate the anomaly in ARF_{atm} values during the peak of the fire season. The anomaly is determined by subtracting the monthly mean ARF_{atm} for April across all other years (2011 to 2024) from the monthly mean ARF_{atm} values in the wildfire event years. Positive anomalies in ARF_{atm} values are observed over the southern part of the HTP region (Figure 9), indicating that the intense smoke emitted by wildfires on the southern slopes of the Himalayas exerts a positive radiative forcing on the atmosphere, potentially contributing to atmospheric warming. It should be noted that the aerosol radiative forcing data from CERES represent the radiative characteristics of all aerosols in the atmosphere, which are not limited to smoke aerosol but also encompasses the effects of other aerosol types. As a result, the values exhibit a broad range of variability.
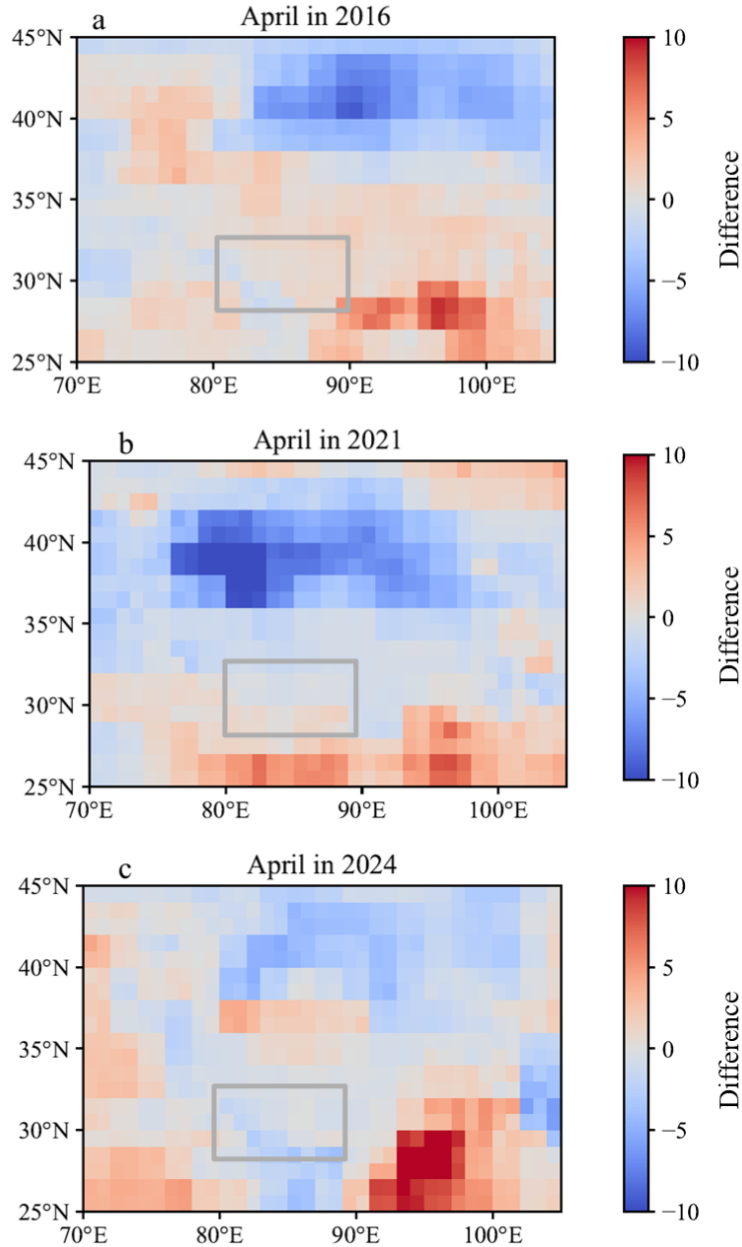
Figure 9. CERES satellite-derived differences in ARF (W m⁻²) between intense wildfire events (2016 (a), 2021 (b), and 2024 (c)) and the April monthly averages for the other years from 2011 to 2024.

4   Conclusion and Perspective

Incorporating long-term MODIS fire products, ground-based and satellite-derived aerosol datasets, and model simulations, this study investigates the predominant biomass burning species affecting the HTP region and its potential impact on atmospheric warming. The AOD at 500 nm from AERONET sites in Pokhara, QOMS, and Nam Co displayed distinct interannual and seasonal patterns, correlating with fire pixel counts and FRP, particularly peaking from March to May with notable fire events in 2016, 2021, and 2024. Strong positive correlations were observed between

Himalayas' fire pixel counts and both total AOD and fine-mode AOD at Pokhara (r = 0.76 and r = 0.73, respectively; p < 0.001) and Nam Co (r = 0.69 and r = 0.68, respectively; p < 0.001) throughout the 2011–2024 period. Conversely, no consistent trends or significant correlations were detected over the IGP. Combined with forward trajectory analyses, these findings indicate that wildfires on the southern slopes of the Himalayas are the primary driver of aerosol loading over the HTP region.

For the southern HTP region, multi-year-average extinction values of various aerosol types during peak fire seasons (March and April, 2011–2023) were derived from the CALIPSO L2 aerosol profile product. The extinction coefficient of smoke aerosol was markedly higher in 2021, corresponding with the interannual variability in fire pixel counts. During the peak fire season, smoke was especially abundant at altitudes of 6–8 km in the mid-troposphere, with elevated extinction coefficient in 2021. CALIPSO observations during specific wildfire events indicated that smoke aerosols were the major aerosol type at altitudes of 6–10 km. The intense wildfire activity in 2021 likely raised the mid-tropospheric temperatures and altered the vertical temperature structure, as reflected in reduced absolute temperature lapse rate values (slope K)—the rate at which temperature decreases with increasing altitude—observed at the QOMS, SETS, and Naqu stations compared to 2022. Utilizing realistic CALIPSO-derived smoke extinction profiles, heating rates were calculated with the SBDART model under scenarios with and without smoke aerosols. The presence of smoke aerosols enhanced atmospheric absorption, leading to layer warming with the heating rate increasing by 0.38 to 1.32 K day^{-1} (mean = 0.64 ± 0.25 K day^{-1}) in the middle troposphere compared to the scenario without smoke aerosols. Additionally, average warming within the smoke layer was approximately 15.03–22.43 W m^{-2}, supported by the low SSA values observed at QOMS and Pokhara sites, highlighting the warming effect of smoke aerosols.

The impact of aerosols is important for climate change, the hydrological cycle, and the cryosphere in the HTP region. The mid-troposphere warming induced by smoke aerosols, as observed in our study, is a significant factor contributing to changes in regional atmospheric stability and modulating surface temperatures. This warming is also expected to influence the melting dynamics of snowpacks and glaciers, as well as precipitation patterns, thereby impacting water availability and quality in the AWT to some extent. A more comprehensive investigation into the atmospheric heating and cooling processes induced by various aerosol types, along with the

496 corresponding vertical temperature structure in the HTP, is crucial for advancing our understanding

497 of how the climate responds to aerosol effects in the context of global warming.

498

499 **Data availability**

500   The AERONET dataset is accessible at https://aeronet.gsfc.nasa.gov/ (NASA, 2016). The

501 MODIS Collection 6 Hotspot / Active Fire Detections MCD14ML is distributed by NASA Fire

502 Information for Resource Management System (FIRMS), and can be accessed

503 at https://earthdata.nasa.gov/firms (Lancemodis, 2021; NASA, 2021). CALIPSO's Level 2 LiDAR

504 Vertical Feature Mask (CAL_LID_L2_VFM-Standard-V4-20) and 5 km Aerosol Profile products

505 (CAL_LID_L2_05kmAPro-Standard-V4-20) are available through Atmospheric Science Data

506 Centre (ASDC) at https://subset.larc.nasa.gov/calipso/login.php. The CERES SYN1deg-Day Terra-

507 Aqua-MODIS Edition 4A (SYN1deg Level 3) dataset can be obtained from

508 https://ceres.larc.nasa.gov/data/ (NASA/LARC/SD/ASDC, 2017). The elevation data from GEneral

509 Bathymetric Chart of the Ocean (GEBCO's) current gridded bathymetric dataset can be downloaded

510 from https://www.gebco.net/. The MODIS Land Cover Type Yearly Climate Modeling Grid (CMG),

511 including the dominant land cover type product (MCD12C1), is available through the Level-1 and

512 Atmosphere Archive & Distribution System Distributed Active Archive Center (LAADS DAAC) at

513 https://ladsweb.modaps.eosdis.nasa.gov/search/order/1. Ground-based microwave radiometers for

514 temperature over Tibetan Plateau (Ma Yaoming, 2024), along with the Tibetan Plateau boundary

515 dataset (Yili, 2019), are provided by the National Tibetan Plateau Data Center

516 (http://data.tpdc.ac.cn). The HYSPLIT model is available via the NOAA's Air Resources

517 Laboratory's (ARL) website (https://www.ready.noaa.gov/HYSPLIT.php).

518 **Author contributions**

519 CZ designed and conceived the research. QP drafted the initial manuscript. YY and AC contributed

520 to the SBDART method. ZC provided a portion of the data. CZ, QP, YY, AC, XW, HZ, and GW

521 reviewed and edited the manuscript.

522 **Competing interests**

523   The authors declare that they have no conflict of interests.

524   **Acknowledgement**

525   This work is supported by the National Key Research and Development Program of China
526   (grant number 24YFF0809402), the Yunnan Southwest United Graduate School Science and
527   Technology Special Project (grant number 202302AP370003). We are grateful to the AERONET
528   team for providing validation data and thank Pawan Gupta, Elena S. Lind, and their staff for
529   establishing and maintaining the Pokhara site in this investigation. We are deeply appreciative of
530   the MODIS, CALIPSO, CERES, and NASA's FIRMS teams for granting access to their valuable
531   data. Additionally, we acknowledge the NOAA ARL for providing the HYSPLIT transport model
532   and the Data Archive of Tracer Experiments and Meteorology, which were essential to this study.
533   Finally, we would like to acknowledge the source of the GEBCO Grid and the National Tibetan
534   Plateau Data Center for their invaluable contributions.

535   **References**

536   Andreae, M. O.: Emission of trace gases and aerosols from biomass burning – an updated
537   assessment, Atmos. Chem. Phys., 19, 8523-8546, https://doi.org/10.5194/acp-19-8523-2019,
538   2019.

539   Bhardwaj, P., Naja, M., Kumar, R., and Chandola, H. C.: Seasonal, interannual, and long-term
540   variabilities in biomass burning activity over South Asia, Environmental Science and Pollution
541   Research, 23, 4397-4410, https://doi.org/10.1007/s11356-015-5629-6, 2016.

542   Bhattarai, H., Wu, G., Zheng, X., Zhu, H., Gao, S., Zhang, Y.-L., Widory, D., Ram, K., Chen, X.,
543   Wan, X., Pei, Q., Pan, Y., Kang, S., and Cong, Z.: Wildfire-Derived Nitrogen Aerosols Threaten
544   the Fragile Ecosystem in Himalayas and Tibetan Plateau, Environmental Science & Technology,
545   57, 9243-9251, https://doi.org/10.1021/acs.est.3c01541, 2023.

546   Chen, D.: Assessment of past, present and future environmental changes on the Tibetan Plateau (in
547   Chinese   with   English   abstract),   Chin.   Sci.   Bull.,   60,   3025-3035,
548   https://doi.org/10.1360/N972014-01370, 2015.

549   Chen, X., Liu, Y., Ma, Y., Ma, W., Xu, X., Cheng, X., Li, L., Xu, X., and Wang, B.: TP-PROFILE:
550   Monitoring the Thermodynamic Structure of the Troposphere over the Third Pole, Advances in

Atmospheric Sciences, 41, 1264-1277, https://doi.org/10.1007/s00376-023-3199-y, 2024.

Cong, Z., Kang, S., Kawamura, K., Liu, B., Wan, X., Wang, Z., Gao, S., and Fu, P.: Carbonaceous aerosols on the south edge of the Tibetan Plateau: concentrations, seasonality and sources, Atmos. Chem. Phys., 15, 1573-1584, https://doi.org/10.5194/acp-15-1573-2015, 2015.

Dubovik, O., Smirnov, A., Holben, B. N., King, M. D., Kaufman, Y. J., Eck, T. F., and Slutsker, I.: Accuracy assessments of aerosol optical properties retrieved from Aerosol Robotic Network (AERONET) Sun and sky radiance measurements, Journal of Geophysical Research: Atmospheres, 105, 9791-9806, https://doi.org/10.1029/2000JD900040, 2000.

Dumka, U. C., Saheb, S. D., Kaskaoutis, D. G., Kant, Y., and Mitra, D.: Columnar aerosol characteristics and radiative forcing over the Doon Valley in the Shivalik range of northwestern Himalayas, Environ Sci Pollut Res Int, 23, 25467-25484, https://doi.org/10.1007/s11356-016-7766-y, 2016.

Holben, B. N., Eck, T. F., Slutsker, I., Tanré, D., Buis, J. P., Setzer, A., Vermote, E., Reagan, J. A., Kaufman, Y. J., Nakajima, T., Lavenu, F., Jankowiak, I., and Smirnov, A.: AERONET—A Federated Instrument Network and Data Archive for Aerosol Characterization, Remote Sensing of Environment, 66, 1-16, https://doi.org/10.1016/S0034-4257(98)00031-5, 1998.

Holben, B. N., Tanré, D., Smirnov, A., Eck, T. F., Slutsker, I., Abuhassan, N., Newcomb, W. W., Schafer, J. S., Chatenet, B., Lavenu, F., Kaufman, Y. J., Castle, J. V., Setzer, A., Markham, B., Clark, D., Frouin, R., Halthore, R., Karneli, A., O'Neill, N. T., Pietras, C., Pinker, R. T., Voss, K., and Zibordi, G.: An emerging ground-based aerosol climatology: Aerosol optical depth from AERONET, Journal of Geophysical Research: Atmospheres, 106, 12067-12097, https://doi.org/10.1029/2001JD900014, 2001.

Immerzeel, W. W., van Beek, L. P. H., and Bierkens, M. F. P.: Climate Change Will Affect the Asian Water Towers, Science, 328, 1382-1385, https://doi.org/10.1126/science.1183188, 2010.

IPCC: Summary for Policymakers, in: Synthesis Report. Contribution of Working Groups I, II and III to the Sixth Assessment Report of the Intergovernmental Panel on Climate Change [Core Writing Team, H. Lee and J. Romero (eds.)], edited by: Intergovernmental Panel on Climate, C., Geneva, Switzerland, 1-34, https://doi.org/10.59327/IPCC/AR6-9789291691647.001, 2023a.

IPCC: The Earth's Energy Budget, Climate Feedbacks and Climate Sensitivity, in: Climate Change

2021 – The Physical Science Basis: Working Group I Contribution to the Sixth Assessment Report of the Intergovernmental Panel on Climate Change, edited by: Intergovernmental Panel on Climate, C., Cambridge University Press, Cambridge, 923-1054, https://doi.org/10.1017/9781009157896.009, 2023b.

Kang, S., Zhang, Y., Qian, Y., and Wang, H.: A review of black carbon in snow and ice and its impact on the cryosphere, Earth-Science Reviews, 210, 103346, https://doi.org/10.1016/j.earscirev.2020.103346, 2020.

Kang, S., Zhang, Q., Qian, Y., Ji, Z., Li, C., Cong, Z., Zhang, Y., Guo, J., Du, W., Huang, J., You, Q., Panday, A. K., Rupakheti, M., Chen, D., Gustafsson, Ö., Thiemens, M. H., and Qin, D.: Linking atmospheric pollution to cryospheric change in the Third Pole region: current progress and future prospects, National Science Review, 6, 796-809, https://doi.org/10.1093/nsr/nwz031, 2019.

Kang, L., Huang, J., Chen, S., and Wang, X.: Long-term trends of dust events over Tibetan Plateau during 1961–2010, Atmospheric Environment, 125, 188-198, https://doi.org/10.1016/j.atmosenv.2015.10.085, 2016.

Kaskaoutis, D. G., Kumar, S., Sharma, D., Singh, R. P., Kharol, S. K., Sharma, M., Singh, A. K., Singh, S., Singh, A., and Singh, D.: Effects of crop residue burning on aerosol properties, plume characteristics, and long-range transport over northern India, Journal of Geophysical Research: Atmospheres, 119, 5424-5444, https://doi.org/10.1002/2013jd021357, 2014.

Kedia, S., Ramachandran, S., Kumar, A., and Sarin, M. M.: Spatiotemporal gradients in aerosol radiative forcing and heating rate over Bay of Bengal and Arabian Sea derived on the basis of optical, physical, and chemical properties, Journal of Geophysical Research: Atmospheres, 115, https://doi.org/10.1029/2009JD013136, 2010.

Kim, M.-H., Omar, A. H., Tackett, J. L., Vaughan, M. A., Winker, D. M., Trepte, C. R., Hu, Y., Liu, Z., Poole, L. R., Pitts, M. C., Kar, J., and Magill, B. E.: The CALIPSO version 4 automated aerosol classification and lidar ratio selection algorithm, Atmospheric Measurement Techniques, 11, 6107-6135, https://doi.org/10.5194/amt-11-6107-2018, 2018.

Koren, I., Kaufman, Y. J., Remer, L. A., and Martins, J. V.: Measurement of the effect of Amazon smoke on inhibition of cloud formation, Science, 303, 1342-1345,

609   https://doi.org/10.1126/science.1089424, 2004.

610 Krishnan, R., Shrestha, A. B., Ren, G., Rajbhandari, R., Saeed, S., Sanjay, J., Syed, M. A., Vellore,

611   R., Xu, Y., You, Q., and Ren, Y.: Unravelling Climate Change in the Hindu Kush Himalaya: Rapid

612   Warming in the Mountains and Increasing Extremes, in: The Hindu Kush Himalaya Assessment:

613   Mountains, Climate Change, Sustainability and People, edited by: Wester, P., Mishra, A.,

614   Mukherji, A., and Shrestha, A. B., Springer International Publishing, Cham, 57-97,

615   https://doi.org/10.1007/978-3-319-92288-1_3, 2019.

616 LANCEMODIS: MODIS/Aqua Terra Thermal Anomalies/Fire locations 1km FIRMS NRT (Vector

617   data). MODAPS at NASA/GSFC: The Land, Atmosphere Near real-time Capability for EOS

618   (LANCE).   https://earthdata.nasa.gov/earth-observation-data/near-real-time/firms/active-fire-

619   data. [dataset], 2021.

620 Lau, W. K. M. and Kim, K. M.: Impact of snow-darkening by deposition of light-absorbing aerosols

621   on snow cover in the Himalaya-Tibetan-Plateau and influence on the Asian Summer monsoon: A

622   possible mechanism for the Blanford Hypothesis, Atmosphere (Basel), 9, 438,

623   https://doi.org/10.3390/atmos9110438, 2018.

624 Li, C., Bosch, C., Kang, S., Andersson, A., Chen, P., Zhang, Q., Cong, Z., Chen, B., Qin, D., and

625   Gustafsson, Ö.: Sources of black carbon to the Himalayan–Tibetan Plateau glaciers, Nature

626   Communications, 7, 12574, https://doi.org/10.1038/ncomms12574, 2016.

627 Li, F., Wan, X., Wang, H., Orsolini, Y. J., Cong, Z., Gao, Y., and Kang, S.: Arctic sea-ice loss

628   intensifies aerosol transport to the Tibetan Plateau, Nature Climate Change, 10, 1037-1044,

629   https://doi.org/10.1038/s41558-020-0881-2, 2020.

630 Li, J., Carlson, B. E., Yung, Y. L., Lv, D., Hansen, J., Penner, J. E., Liao, H., Ramaswamy, V., Kahn,

631   R. A., Zhang, P., Dubovik, O., Ding, A., Lacis, A. A., Zhang, L., and Dong, Y.: Scattering and

632   absorbing aerosols in the climate system, Nature Reviews Earth & Environment, 3, 363-379,

633   https://doi.org/10.1038/s43017-022-00296-7, 2022.

634 Liu, Y.: Atmospheric response and feedback to radiative forcing from biomass burning in tropical

635   South America, Agricultural and Forest Meteorology, 133, 40-53,

636   https://doi.org/10.1016/j.agrformet.2005.03.011, 2005.

637 Liu, Z., Liu, D., Huang, J., Vaughan, M., Uno, I., Sugimoto, N., Kittaka, C., Trepte, C., Wang, Z.,

638   Hostetler, C., and Winker, D.: Airborne dust distributions over the Tibetan Plateau and

639   surrounding areas derived from the first year of CALIPSO lidar observations, Atmos. Chem.

640   Phys., 8, 5045-5060, https://doi.org/10.5194/acp-8-5045-2008, 2008.

641   Lu, Q., Liu, C., Zhao, D., Zeng, C., Li, J., Lu, C., Wang, J., and Zhu, B.: Atmospheric heating rate

642   due to black carbon aerosols: Uncertainties and impact factors, Atmospheric Research, 240,

643   104891, https://doi.org/10.1016/j.atmosres.2020.104891, 2020.

644   Lüthi, Z. L., Škerlak, B., Kim, S. W., Lauer, A., Mues, A., Rupakheti, M., and Kang, S.: Atmospheric

645   brown clouds reach the Tibetan Plateau by crossing the Himalayas, Atmos. Chem. Phys., 15,

646   6007-6021, https://doi.org/10.5194/acp-15-6007-2015, 2015.

647   Ma Yaoming, C. X.: TP-PROFILE monitoring of the troposphere over the Tibetan Plateau (2021-

648   2022), National Tibetan Plateau Data Center [dataset],

649   https://doi.org/10.11888/Atmos.tpdc.272995, 2024.

650   Menon, S., Hansen, J., Nazarenko, L., and Luo, Y.: Climate Effects of Black Carbon Aerosols in

651   China and India, Science, 297, 2250-2253, https://doi.org/10.1126/science.1075159, 2002.

652   Moorthy, K. K., Nair, V. S., Babu, S. S., and Satheesh, S. K.: Spatial and vertical heterogeneities in

653   aerosol properties over oceanic regions around India: Implications for radiative forcing, Quarterly

654   Journal of the Royal Meteorological Society, 135, 2131-2145, https://doi.org/10.1002/qj.525,

655   2009.

656   NASA: AEROSOL OPTICAL DEPTH (V3) – SOLAR and AEROSOL INVERSIONS (V3),

657   Goddard Space Flight Center, USA, https://aeronet.gsfc.nasa.gov/ [dataset], 2016.

658   NASA: VIIRS (NOAA-21/JPSS-2) I Band 375 m Active Fire Product NRT (Vector data). NASA

659   LANCE MODIS at the MODAPS.

660   https://doi.org/10.5067/FIRMS/MODIS/MCD14DL.NRT.0061 [dataset], 2021.

661   NASA/LARC/SD/ASDC: CERES and GEO-Enhanced TOA, Within-Atmosphere and Surface

662   Fluxes, Clouds and Aerosols Daily Terra-Aqua Edition4A [dataset], 2017.

663   O'Neill, N. T., Eck, T. F., Smirnov, A., Holben, B. N., and Thulasiraman, S.: Spectral discrimination

664   of coarse and fine mode optical depth, Journal of Geophysical Research: Atmospheres, 108,

665   https://doi.org/10.1029/2002JD002975, 2003.

666   Omar, A. H., Winker, D. M., Kittaka, C., Vaughan, M. A., Liu, Z. Y., Hu, Y. X., Trepte, C. R., Rogers,

R. R., Ferrare, R. A., Lee, K. P., Kuehn, R. E., and Hostetler, C. A.: The CALIPSO Automated Aerosol Classification and Lidar Ratio Selection Algorithm, Journal of Atmospheric and Oceanic Technology, 26, 1994-2014, https://doi.org/10.1175/2009jtecha1231.1, 2009.

Panicker, A. S., Pandithurai, G., Safai, P. D., Dipu, S., and Lee, D.-I.: On the contribution of black carbon to the composite aerosol radiative forcing over an urban environment, Atmospheric Environment, 44, 3066-3070, https://doi.org/10.1016/j.atmosenv.2010.04.047, 2010.

Pant, P., Hegde, P., Dumka, U. C., Sagar, R., Satheesh, S. K., Moorthy, K. K., Saha, A., and Srivastava, M. K.: Aerosol characteristics at a high-altitude location in central Himalayas: Optical properties and radiative forcing, Journal of Geophysical Research: Atmospheres, 111, https://doi.org/10.1029/2005JD006768, 2006.

Pokharel, M., Guang, J., Liu, B., Kang, S., Ma, Y., Holben, B. N., Xia, X. a., Xin, J., Ram, K., Rupakheti, D., Wan, X., Wu, G., Bhattarai, H., Zhao, C., and Cong, Z.: Aerosol Properties Over Tibetan Plateau From a Decade of AERONET Measurements: Baseline, Types, and Influencing Factors, Journal of Geophysical Research: Atmospheres, 124, 13357-13374, https://doi.org/10.1029/2019jd031293, 2019.

Rai, M., Mahapatra, P. S., Gul, C., Kayastha, R. B., Panday, A. K., and Puppala, S. P.: Aerosol Radiative Forcing Estimation over a Remote High-altitude Location (~4900 masl) near Yala Glacier, Nepal, Aerosol and Air Quality Research, 19, 1872-1891, https://doi.org/10.4209/aaqr.2018.09.0342, 2019.

Ramachandran, S. and Rupakheti, M.: Inter-annual and seasonal variations in optical and physical characteristics of columnar aerosols over the Pokhara Valley in the Himalayan foothills, Atmospheric Research, 248, 105254, https://doi.org/10.1016/j.atmosres.2020.105254, 2021.

Ramachandran, S., Rupakheti, M., and Lawrence, M. G.: Black carbon dominates the aerosol absorption over the Indo-Gangetic Plain and the Himalayan foothills, Environment International, 142, 105814, https://doi.org/10.1016/j.envint.2020.105814, 2020.

Ramachandran, S., Rupakheti, M., Cherian, R., and Lawrence, M. G.: Aerosols heat up the Himalayan climate, Science of The Total Environment, 894, 164733, https://doi.org/10.1016/j.scitotenv.2023.164733, 2023.

Ramanathan, V., Crutzen, P. J., Kiehl, J. T., and Rosenfeld, D.: Atmosphere - Aerosols, climate, and

696   the hydrological cycle, Science, 294, 2119-2124, https://doi.org/10.1126/science.1064034, 2001a.

697   Ramanathan, V., Ramana, M. V., Roberts, G., Kim, D., Corrigan, C., Chung, C., and Winker, D.:

698   Warming trends in Asia amplified by brown cloud solar absorption, Nature, 448, 575-578,

699   https://doi.org/10.1038/nature06019, 2007.

700   Ramanathan, V., Crutzen, P. J., Lelieveld, J., Mitra, A. P., Althausen, D., Anderson, J., Andreae, M.

701   O., Cantrell, W., Cass, G. R., Chung, C. E., Clarke, A. D., Coakley, J. A., Collins, W. D., Conant,

702   W. C., Dulac, F., Heintzenberg, J., Heymsfield, A. J., Holben, B., Howell, S., Hudson, J.,

703   Jayaraman, A., Kiehl, J. T., Krishnamurti, T. N., Lubin, D., McFarquhar, G., Novakov, T., Ogren,

704   J. A., Podgorny, I. A., Prather, K., Priestley, K., Prospero, J. M., Quinn, P. K., Rajeev, K., Rasch,

705   P., Rupert, S., Sadourny, R., Satheesh, S. K., Shaw, G. E., Sheridan, P., and Valero, F. P. J.: Indian

706   Ocean Experiment: An integrated analysis of the climate forcing and effects of the great Indo-

707   Asian haze, Journal of Geophysical Research: Atmospheres, 106, 28371-28398,

708   https://doi.org/10.1029/2001JD900133, 2001b.

709   Ricchiazzi, P., Yang, S., Gautier, C., and Sowle, D.: SBDART: A Research and Teaching Software

710   Tool for Plane-Parallel Radiative Transfer in the Earth's Atmosphere, Bulletin of the American

711   Meteorological Society, 79, 2101-2114, https://doi.org/10.1175/1520-

712   0477(1998)079<2101:SARATS>2.0.CO;2, 1998.

713   Satheesh, S. K. and Ramanathan, V.: Large differences in tropical aerosol forcing at the top of the

714   atmosphere and Earth's surface, Nature, 405, 60-63, https://doi.org/10.1038/35011039, 2000.

715   Stamnes, K., Tsay, S. C., and Laszlo, I.: DISORT, a General-Purpose Fortran Program for Discrete-

716   Ordinate-Method Radiative Transfer in Scattering and Emitting Layered Media: Documentations

717   of Methodology, 2000.

718   Stein, A. F., Draxler, R. R., Rolph, G. D., Stunder, B. J. B., Cohen, M. D., and Ngan, F.: NOAA's

719   HYSPLIT Atmospheric Transport and Dispersion Modeling System, Bulletin of the American

720   Meteorological Society, 96, 2059-2077, https://doi.org/10.1175/BAMS-D-14-00110.1, 2015.

721   Stocker, M., Ladstädter, F., and Steiner, A. K.: Observing the climate impact of large wildfires on

722   stratospheric temperature, Scientific Reports, 11, https://doi.org/10.1038/s41598-021-02335-7,

723   2021.

724   Tian, P., Yu, Z., Cui, C., Huang, J., Kang, C., Shi, J., Cao, X., and Zhang, L.: Atmospheric aerosol

size distribution impacts radiative effects over the Himalayas via modulating aerosol single-scattering albedo, npj Climate and Atmospheric Science, 6, 54, https://doi.org/10.1038/s41612-023-00368-5, 2023.

Vadrevu, K. P., Ellicott, E., Giglio, L., Badarinath, K. V. S., Vermote, E., Justice, C., and Lau, W. K. M.: Vegetation fires in the himalayan region – Aerosol load, black carbon emissions and smoke plume heights, Atmospheric Environment, 47, 241-251, https://doi.org/10.1016/j.atmosenv.2011.11.009, 2012.

Venkataraman, C., Habib, G., Kadamba, D., Shrivastava, M., Leon, J. F., Crouzille, B., Boucher, O., and Streets, D. G.: Emissions from open biomass burning in India: Integrating the inventory approach with high-resolution Moderate Resolution Imaging Spectroradiometer (MODIS) active-fire and land cover data, Global Biogeochemical Cycles, 20, https://doi.org/10.1029/2005GB002547, 2006.

Wang, S., Zhao, W., Liu, Q., Zhou, J., Crumeyrolle, S., Xu, X., Zhang, C., Ye, C., Zheng, Y., Che, H., and Zhang, W.: Strong Aerosol Absorption and Its Radiative Effects in Lhasa on the Tibetan Plateau, Geophysical Research Letters, 51, https://doi.org/10.1029/2023gl107833, 2024.

Winker, D. M., Pelon, J., Coakley, J. A., Ackerman, S. A., Charlson, R. J., Colarco, P. R., Flamant, P. H., Fu, Q., Hoff, R. M., Kittaka, C., Kubar, T. L., Treut, H. L., McCormick, M. P., Mégie, G., Poole, L. R., Powell, K., Trepte, C. R., Vaughan, M. A., and Wielicki, B. A.: THE CALIPSO MISSION: A Global 3D View of Aerosols and Clouds, Bulletin of the American Meteorological Society, 91, 1211-1229, https://doi.org/10.1175/2010BAMS3009.1, 2010.

Wu, G., Liu, Y., Wang, T., Wan, R., Liu, X., Li, W., Wang, Z., Zhang, Q., Duan, A., and Liang, X.: The Influence of Mechanical and Thermal Forcing by the Tibetan Plateau on Asian Climate, Journal of Hydrometeorology - J HYDROMETEOROL, 8, 10.1175/JHM609.1, 2007.

Wu, G., Wan, X., Gao, S., Fu, P., Yin, Y., Li, G., Zhang, G., Kang, S., Ram, K., and Cong, Z.: Humic-Like Substances (HULIS) in Aerosols of Central Tibetan Plateau (Nam Co, 4730 m asl): Abundance, Light Absorption Properties, and Sources, Environmental Science & Technology, 52, 7203-7211, https://doi.org/10.1021/acs.est.8b01251, 2018.

Yang, J., Ji, Z., Kang, S., and Tripathee, L.: Contribution of South Asian biomass burning to black carbon over the Tibetan Plateau and its climatic impact, Environmental Pollution, 270, 116195,

https://doi.org/10.1016/j.envpol.2020.116195, 2021a.

Yang, J., Kang, S., Hu, Y., Chen, X., and Rai, M.: Springtime biomass burning impacts air quality and climate over the Tibetan Plateau, Atmospheric Environment, 313, 120068, https://doi.org/10.1016/j.atmosenv.2023.120068, 2023.

Yang, X., Zhao, C., Yang, Y., Yan, X., and Fan, H.: Statistical aerosol properties associated with fire events from 2002 to 2019 and a case analysis in 2019 over Australia, Atmospheric Chemistry and Physics, 21, 3833-3853, https://doi.org/10.5194/acp-21-3833-2021, 2021b.

Yao, T., Bolch, T., Chen, D., Gao, J., Immerzeel, W., Piao, S., Su, F., Thompson, L., Wada, Y., Wang, L., Wang, T., Wu, G., Xu, B., Yang, W., Zhang, G., and Zhao, P.: The imbalance of the Asian water tower, Nature Reviews Earth & Environment, 3, 618-632, https://doi.org/10.1038/s43017-022-00299-4, 2022.

Yao, T., Xue, Y., Chen, D., Chen, F., Thompson, L., Cui, P., Koike, T., Lau, W. K. M., Lettenmaier, D., Mosbrugger, V., Zhang, R., Xu, B., Dozier, J., Gillespie, T., Gu, Y., Kang, S., Piao, S., Sugimoto, S., Ueno, K., Wang, L., Wang, W., Zhang, F., Sheng, Y., Guo, W., Ailikun, Yang, X., Ma, Y., Shen, S. S. P., Su, Z., Chen, F., Liang, S., Liu, Y., Singh, V. P., Yang, K., Yang, D., Zhao, X., Qian, Y., Zhang, Y., and Li, Q.: Recent Third Pole's Rapid Warming Accompanies Cryospheric Melt and Water Cycle Intensification and Interactions between Monsoon and Environment: Multidisciplinary Approach with Observations, Modeling, and Analysis, Bulletin of the American Meteorological Society, 100, 423-444, https://doi.org/10.1175/bams-d-17-0057.1, 2019.

Yili, Z.: Integration dataset of Tibet Plateau boundary, National Tibetan Plateau Data Center [dataset], https://doi.org/10.11888/Geogra.tpdc.270099, 2019.

You, C. and Xu, C.: Himalayan glaciers threatened by frequent wildfires, Nature Geoscience, 15, 956-957, https://doi.org/10.1038/s41561-022-01076-0, 2022.

You, C., Yao, T., and Xu, C.: Recent Increases in Wildfires in the Himalayas and Surrounding Regions Detected in Central Tibetan Ice Core Records, Journal of Geophysical Research: Atmospheres, 123, 3285-3291, https://doi.org/10.1002/2017jd027929, 2018.

Yu, P., Davis, S. M., Toon, O. B., Portmann, R. W., Bardeen, C. G., Barnes, J. E., Telg, H., Maloney, C., and Rosenlof, K. H.: Persistent Stratospheric Warming Due to 2019–2020 Australian Wildfire

783   Smoke, Geophysical Research Letters, 48, https://doi.org/10.1029/2021gl092609, 2021.

784   Zhao, C. F., Yang, Y. K., Fan, H., Huang, J. P., Fu, Y. F., Zhang, X. Y., Kang, S. C., Cong, Z. Y.,

785   Letu, H., and Menenti, M.: Aerosol characteristics and impacts on weather and climate over the

786   Tibetan Plateau, National Science Review, 7, 492-+, https://doi.org/10.1093/nsr/nwz184, 2020.

787   Zheng, C., Zhao, C., Zhu, Y., Wang, Y., Shi, X., Wu, X., Chen, T., Wu, F., and Qiu, Y.: Analysis of

788   influential factors for the relationship between PM2.5 and AOD in Beijing, Atmos. Chem. Phys.,

789   17, 13473-13489, https://doi.org/10.5194/acp-17-13473-2017, 2017.